Figures and Tables.

Resolution shells (Å)		Dataset #1 λ_1= 1.00695 Å		Dataset #2 λ_2= 1.00923 Å	
Lower	Upper	Average I	Linear R-factor	Average I	Linear R-factor
50	8.18	2914.5	0.053	2210.0	0.058
8.17	6.49	574.2	0.061	357.6	0.069
6.48	5.67	231.3	0.078	128.2	0.097
5.66	5.16	212.7	0.080	116.9	0.110
5.15	4.79	215.8	0.087	116.0	0.127
4.78	4.50	198.0	0.100	102.6	0.151
4.49	4.28	138.2	0.126	66.0	0.208
4.27	4.09	92.8	0.167	43.0	0.289
4.08	3.94	58.9	0.257	22.7	0.489
3.93	3.80	53.9	0.347	28.1	0.578
All reflections		477.0	0.072	315.7	0.082

Table S1. Statistics describing two original datasets of mercury labeled drug-free mouse Pgp ("Crystal 2") collected at two x-ray wavelengths (λ_1 and λ_2) near the Hg LIII absorption edge for MAD phasing. The table was generated from original datasets collected for the mouse Pgp structure published by Aller et al (*1*). Radiation damage is particularly evident for the last two resolution shells of Dataset #2 (highlighted in yellow and red). Values of ≥ 0.6 are typically considered random.

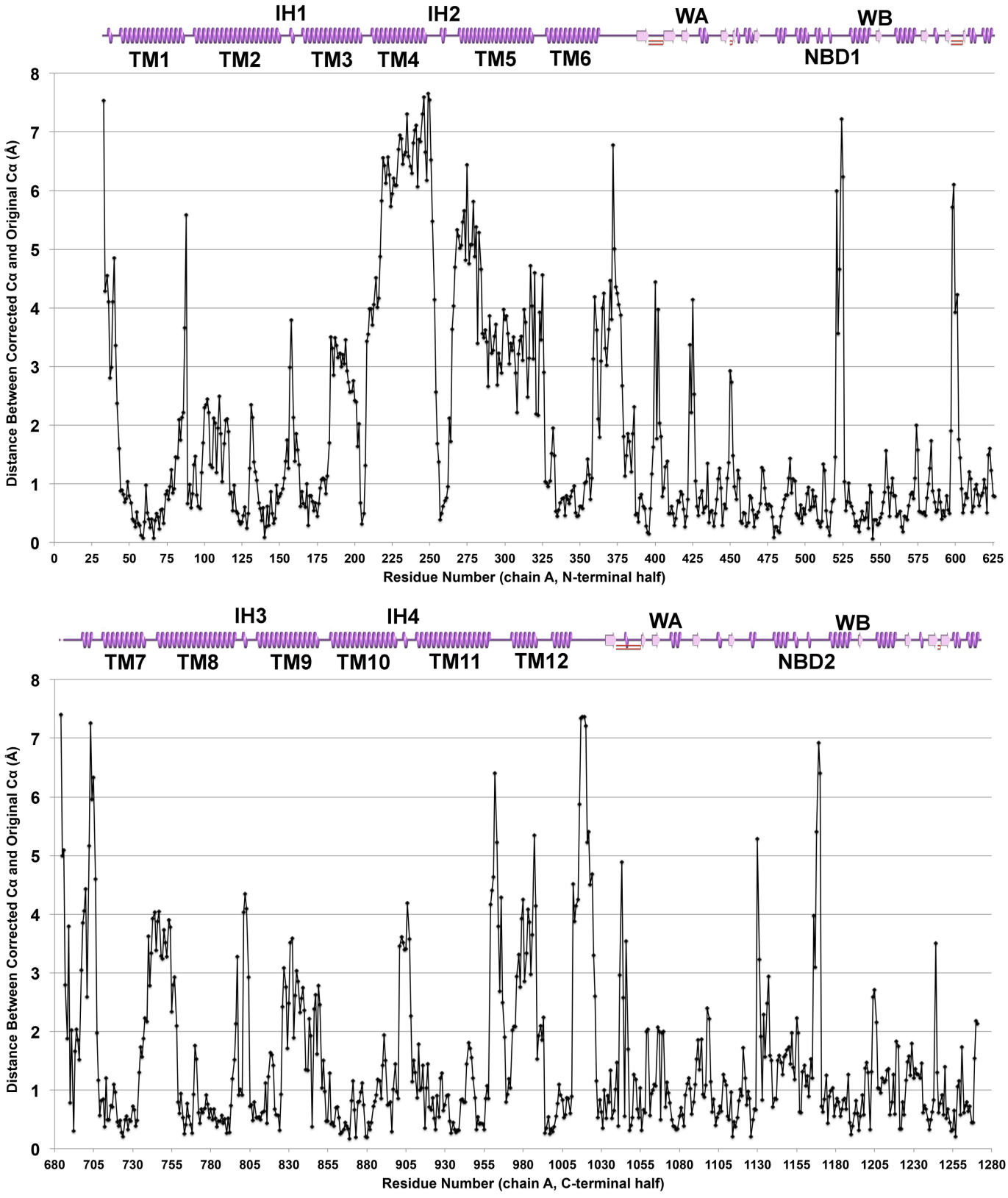

Figure S1. Plot of amino acid residue number versus distance between corrected Cα and original Cα. Secondary structure assignment and structural features of P-glycoprotein are highlighted above the graphs (transmembrane helix, TM, intracellular helix, IH, nucleotide binding domain, NBD, Walker A, WA and Walker B, WB). For simplicity, the plot is for "molecule A" of the asymmetric unit since similar values were obtained for "molecule B" due to non-crystallographic symmetry enforced during refinement.

Detailed Changes to Mouse P-glycoprotein X-ray Crystal Structure (unless explicitly stated, "density" referred to below represents experimental electron density produced from our newly phased map, contoured at 1 σ; old model (3G5U) is always shown in grey, new model (4M1M) is always shown in red):

1) **Elbow Helix 1 (EH1):** The N-terminal "elbow" helix required a rotation of approximately 90˚ (~ one-residue shift in registry) in order to correctly model the large side chains of Phe39 and Tyr41 (see **Fig. S2, panels A and B**) into clear experimental density. Side chains for these two residues were previously modeled in positions unaccounted for by any electron density. Following corrections at the C-terminus of TM6 (discussed below), electron density for three more residues (30-32) was evident for modeling a new N-terminal coil of mouse Pgp. Contiguous electron density connecting the close side chains of Arg40 and Asp366 revealed a salt bridge with the N-terminal elbow and the bottom of TM6 (see **Fig. S2 panel C**).

2) **Transmembrane Helix 1 (TM1):** The helical backbone of TM1 remains essentially unchanged, although the start of the helix was adjusted to allow a better fit of Trp44 (see **Fig. S3, panel A**) into side chain density. A different rotameric configuration of Tyr49 (Panel B) was chosen to fit into very clear density. A slight adjustment of the backbone was made to allow Met74 (see **Fig. S3 panel C**) to fit into clear density.

3) **Transmembrane Helix 2 (TM2):** TM2 required a minor rigid body counterclockwise rotation (looking down from the N-terminus of the helix) of about 15 degrees to allow improved fit of side chains for residues 102-117 (see **Fig. S4, panels A, B and C**) and ending at a Gly118-Ala119-Gly120 constriction. Phe131 and Trp132 were modeled incorrectly due to an unwarranted bulge of the helical backbone for Trp132. A slight adjustment of backbone and choice of proper rotamers allowed good fitting of Phe131 and Trp132 into very clear density (see **Fig. S4 panel D**). The position and registry of the remainder of TM2 (residues 133-153) remain essentially unchanged. A proper rotamer of Phe148 was selected to fit into very clear density (see **Fig. S4 panel E**).

4) **Intracellular Helix 1 (IH1):** Significant remodeling of intracellular helix 1 (IH1) was required. The helix of TM2 clearly terminates at Asn153 as revealed by a slendering of the electron density for the 90˚ turn just prior to the start of IH1 (see **Fig. S5, panel A**). Glu155 was previously modeled into a location with no electron density and its side chain hydrogen bonding with itself. Remodeling of the turn as a coil allowed placement of Gln154 and Glu155 into excellent density in which polar contacts with TM helices and Ser370 (NBD1) were revealed (see **Fig. S5, panels B and C**). Regularization of IH1 (residues 155-161) allowed good placement of the side chains into electron density. Van der Waal contacts between the side chains of Gln154, Trp158 and His162 are evident as contiguous electron density above IH1 (see **Fig. S5 panel D**).

5) **Transmembrane Helix 3 (TM3):** <u>The C-terminal half of TM3 required remodeling in the form of ~ 1-residue registry shift (~ 90˚ rotation):</u> Backbone and side chain atoms of TM3 for roughly the first N-terminal half of the helix (residues 164-180) remained essentially unchanged. A break in TM3 helical ideality was clearly evident in our new experimental electron density map at Gly181, Ile182 and Gly183. This "G-X-G" motif is nearly invariant among drug transporters (ABCB1) and lipid flippases (ABCB4), and appears to allow flexibility in the form of a backbone "bulge" at Ile182 and Gly183. Proper modeling of the helical bulge in experimental electron density that also allows the Ile182 side chain to pack in a hydrophobic environment results in a registry shift of approximately one residue (see **Fig. S6**) for the remainder of the helix (184-204) compared to the original modeling.

6) **Extracellular Loop 2 (ECL2) and Transmembrane Helix 4 (TM4):** Jin et al proposed a registry problem in mouse Pgp TM4 based on an alignment with the higher resolution *C. elegans* Pgp structure (*2*). Inspection of the original electron density maps as well as our new experimental map revealed that extracellular loop 2 (ECL2) of mouse Pgp including the large side chain of Trp208 were originally modeled without any convincing electron density representation. Furthermore, Trp208 is conserved among all P-glycoprotein orthologs, and the position of the corresponding residue in *C. elegans* (Trp236) served as an important landmark for remodeling mouse Pgp TM4. We remodeled ECL2 as a shorter loop that fit well in electron density, and also placed the Trp208 side chain into very clear density to start the TM helix (see **Fig. S7, panels A and B**). A canonical helix representing TM4 fit well into the density with the new chosen position of Trp208 and revealed a 4-residue registry shift (~ one entire helical turn) for the entire TM4 (see **Fig. S7 panel C**). TM4 of *C. elegans* Pgp was modeled as a contiguous helix all the way down to the turn into intracellular helix 2 (IH2). The original modeling of mouse Pgp in this region is quite different with the helix breaking prior to IH3 and 8 residues (249-256) modeled as a coil. Careful inspection of our new experimental maps clearly show this region calls for a helix all the way to IH2.

7) **Intracellular Helix 2 (IH2):** IH2 (residues 256-264) remains essentially unchanged because the registry problem of TM4 was corrected at its N-terminus and modeling TM4 C-terminus as a helix picked up the slack, calling for the start of IH2 at the same original residue (Ala256). Fitting Phe263 near the end of IH2 into clear side chain density (see **Fig. S8**) maintains a helix for this addition position compared to the original.

8) **Transmembrane Helix 5 (TM5):** Experimental electron density in our new map can be seen for large side chains throughout the entire span (see **Fig. S9 panels A through I**) of mouse Pgp TM5 (Tyr273, Met295, Phe299, Tyr303, Tyr306, Phe310, Trp311, and Tyr312). Remodeling of TM5 called for a single-residue shift in registry (see **Fig. S9, panel C**) for the entire helix (~ 90˚ clockwise rotation when looking from N- to C-terminus). The single amino acid shift in mouse Pgp TM5 registry is at odds with the three-residue shift proposed by Jin et al based on the *C. elegans* Pgp-1 structure. Notably, the *C. elegans* Pgp-1 structure is open to the cytoplasm by an additional 15 Å compared to mouse Pgp. Since several of the large amino acid side chains of TM5 are conserved between mouse Pgp and *C. elegans* Pgp-1, modeling of each is deemed highly accurate. We propose that the difference between mouse Pgp and *C. elegans* Pgp-1 TM5 reveals a genuine rotation of TM5 as the transporter opens more fully to envelope large substrates. All-atom molecular dynamics simulations are likely to shed more light on the highly flexible nature of these transporters, and identify more specific roles of residues and entire TM helices that relieve overall strain during the transport cycle.

9) **Extracellular Loop 3 (ECL3):** The modeling of extracellular loop 3 (ECL3) was improved by fitting the backbone as well as the side chain of Tyr322 into very clear side chain density (see **Fig. S10**).

10) **Transmembrane Helix 6 (TM6):** Mouse Pgp TM6 remains essentially unchanged. A slight rotation of the helix (less than 5˚) allowed fitting of a proper rotamer of Phe331 into clear side chain density. A very clear “lobster claw” of density is evident for Phe331 and the following drug-binding residue Phe332 (see **Fig. S11, panel A**). Considering the necessary changes to the very N-terminus of mouse Pgp and the elbow helix, the previous modeling of the Tyr359 side chain near the C-terminal end of TM6 results in an excessive steric clash. Careful inspection of improved experimental electron density and the previous modeling of the helix in this region revealed that the helical backbone protruded out of density resulting in the incorrect positioning of the Tyr359 side chain. A “tightening” of the TM6 backbone to fit into density (see **Fig. S11, panel C**) allows a proper rotamer of Tyr359 and all remaining residues of TM6 (360-367) to fit into

electron density (see **Fig. S11, panel B**), including a clearly visible salt bridge between Asp366 and the elbow helix residue Arg40 (see **Fig. S11, panel D**).

11) **TM6-NBD1 connector:** A problem with the modeling of the connection between TM6 and NBD1 was noticed particularly from the incorrect positioning of the Phe374 side chain. Close inspection of new experimental electron density prompted complete remodeling (see **Fig. S12, panels A, B and C**) of this region (residues Lys368 – Gln385).

12) **Nucleotide Binding Domain 1 (NBD1):** The position of the entire NBD1 remains essentially unchanged, although refinement resulted in improvements (see **Fig. S13**) to NBDs at various locations.

13) **Linker region:** Improved phases did not reveal any more density corresponding to residues for the linker region (positions 627-687).

14) **Elbow Helix 2 (EH2):** As with elbow helix 1 (EH1), EH2 required remodeling. Roughly half of the backbone of EH2 (residues 694-702) in the original modeling was completely out of density. Regularization as well as a rotation and translation were required to fit the backbone completely into density (see **Fig. S14**) as well as a significantly improved fit for the side chain of Trp694.

15) **Transmembrane Helix 7 (TM7):** Clear experimental electron density reveals that the start of TM7 was incorrectly modeled since Trp704 had no experimental electron density representation. Density also revealed that the helix should start lower, with Trp704 forming the initial helical hydrogen bonding network. Repositioning Trp704 to start TM7 (see **Fig. S15**) also allowed a perfect fit of the side chain into experimental density. Refinement resulted in minor improvements to TM7 sidechains, but the helical registry remains unchanged.

16) **Extracellular Loop 4 (ECL4) and Transmembrane Helix 8 (TM8):** Experimental electron density from our new map is discontinuous for extracellular loop 3 (ECL3), making it difficult to comment on previous modeling of this region. However, ECL3 is clearly involved in forming crystal contacts and the direct residues involved in contact must, by definition, be reasonably well ordered. Indeed, inspection of our new experimental map reveals clear side chain density for a residue that is in direct contact with the NBD of another Pgp molecule. Pro741 was previously modeled in this position, but has no side chain to make the contact. "Pulling" the loop down, would position Pro740 in this location, resulting in the same problem. Pulling the loop up would place Glu742 in this position, providing a potential solution with a reasonable good fit into the density. Making such a change would result in a one-residue registry shift for the entire TM8, assuming the helix remains ideal over the full span of residues. Careful inspection of new experimental electron density shows that TM8 at residues Leu758 and Gly759 was modeled as a bulge in the helix protruding slightly out of backbone density. A "tightening" of the helix at this point allowed remodeling and registry correction for residues from Glu742 to Glu759. The remainder of TM8 is in proper registry alignment, and includes improvements in the placement of many side chains, including Phe763, Phe771, Phe773, Glu778, Arg785 and Tyr786 (see **Fig. S16 panels A through E**).

17) **Intracellular helix 3 (IH3):** The positioning of IH3 (residues 795-805) is essentially correct, however experimental electron density called for a more regularized helix than what was originally modeled. Re-modeling IH3 as a regular helix resulted in a better side chain fit of Trp799 and Phe800 into density (see **Fig. S17**).

18) **Transmembrane helix 9 (TM9):** The position and registry of TM9 from residues 807-825 remain unchanged. A problem was observed with the previous modeling of residues 825-827 in which the backbone was wound very tight and places the Arg828 side chain in a region with no electron density whatsoever (see **Fig. S18, panel A**) and that also clashes with the new position of Trp694

(see **Fig. S18, panel B**). A slight relaxation of the helix at 825-827 allowed fitting of Arg828 into very nice density that is contiguous with Tyr994 (see **Fig. S18, panel C**), revealing a likely pi-cation interaction with TM8 and TM12. The relaxation of the helix at 825-827 resulted in a ½-residue registry shift (~45˚ rotation) that improved side chain fitting into experimental density for Arg828, Phe833, Gln834, Asn838, Leu839, Thr841, Ile843, Ile844, Leu847 and Tyr849 (see **Fig. S18, panel D**).

19) **Extracellular loop 5 (ECL5):** ECL5 (residues 849-851) was previously modeled with a small portion of the backbone out of electron density and poor density representation for the large sidechain of Trp851. Re-modeling of the loop to fit into density allowed a proper rotameric choice of the Trp851 side chain to fit very well into density (see **Fig. S19**).

20) **Transmembrane helix 10 (TM10):** The position and registry of TM10 (residues 852-898) remains unchanged, although refinement improved the fitting of most of the sidechains (see **Fig. S20**) on this helix.

21) **Intracellular Helix 4 (IH4):** IH4 (residues 899-908) were previously modeled as a coil in the shape of a helix with no proper hydrogen bond network in the backbone. The finding is evidence for an over-refined structure that was subjected to high thermal coefficients without proper restraints. Re-modeling of IH4 allowed perfect fit as a regular helix from residues 899-906 including perfect fit for all side chains including the easy-to-visualize large sidechain of Phe900 (see **Fig. S21**) that previously had no corresponding density. The correction represents a one-amino acid registry correction.

22) **Transmembrane helix 11 (TM11):** The registry for the entire helix of TM11 (residues 909-962) remains unchanged from the original modeling, although refinement resulted in significant improvement in the placing of side chains for Met911, Glu113, Met915, Met928, Phe934, Phe938, Tyr946, Phe955 and Gln962 (see **Fig. S22, panels A, B and C**).

23) **Extracellular loop 6 (ECL6):** The original modeling of the backbone of ECL6 (residues 963-967) strays rather wildly out of experimental electron density (see **Fig. S23 panel B**) as revealed by our new map. Careful inspection reveals that the very C-terminus of TM11 actually calls for another complete turn of a helix, effectively “pulling” more residues of ECL6 toward real density. After completing another helical turn concluding TM11, ECL6 could easily be modeled into the contiguous density that includes a decent fit of the Phe967 side chain into density (see **Fig. S23, panels A and C**).

24) **Transmembrane helix 12 (TM12):** TM12 (residues 968-1010) consists of important drug binding residues, yet is not well conserved between *C. elegans* Pgp-1 and mammalian Pgp orthologs. Careful inspection of experimental electron density revealed that the original modeling of TM12 included a gradual and increasing registry shift which resulted in an offset of a full turn (90˚ rotation) for 12 residues starting at position 976 down to the “break out” loop (Val987) midway through the helix. The problem was corrected by a *de novo* rebuild of residues 968-987, which fit electron density very well particularly for the large side chains of Phe974, Phe979 and Met982 which previously had virtually no density representation (see **Fig. S24, panels A, B and C**). The break out loop was incorrectly modeled as revealed by protrusion of the backbone at residue Asp993 out of density (see **Fig. S24 panel E**). Correct modeling of the breakout loop keeps the remaining residues of the helix (994-1010) essentially the same as they were previously modeled (see **Fig. S24, panel D**).

25) **TM12-NBD2 connector:** The connector (residues 1009-1028) required a complete rebuild since most of the region had poor electron density representation in our new experimental map. Obvious improvements include the backbone of the entire section fitting into electron density as well as good coverage of most side chains including Tyr1017 (see **Fig. S25, panels A and B**).

26) **Nucleotide Binding Domain 2 (NBD2):** The overall positioning of the backbone of NBD2 remains unchanged, however refinement improved the fit of side chains into density, for example: Leu 1109 and Arg1218 (see **Fig. S26, panels A and through C**) as well as the fit of side chains into density that previous had poor electron density representation: Phe1091, Lys 1098, and Phe1119 (see **Fig. S26, panels D through F**).

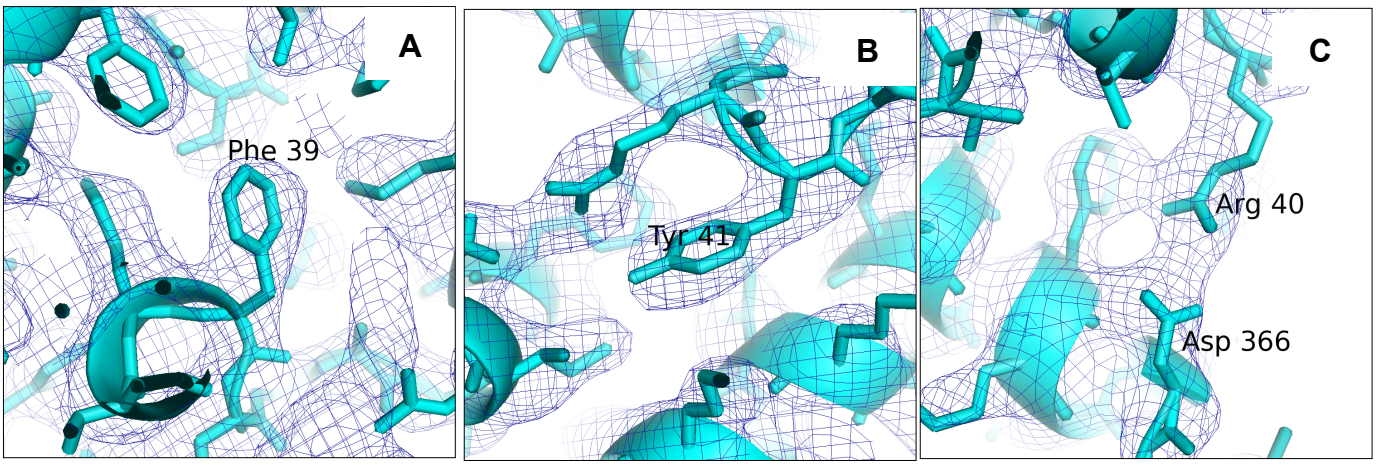

Figure S2. Detailed Changes to "Elbow" Helix 1.

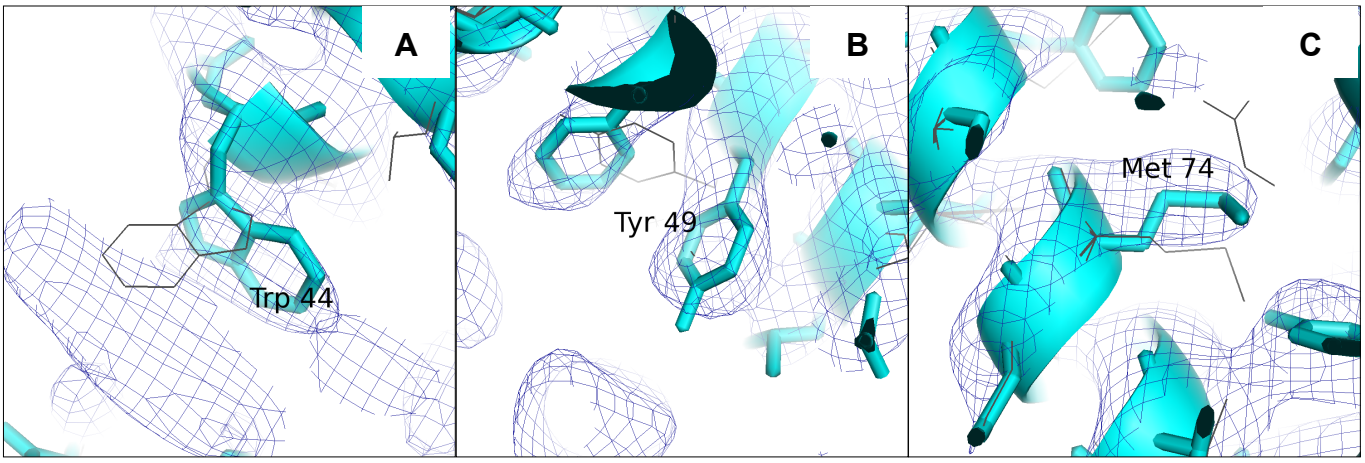

Figure S3. Adjustments to Transmembrane Helix 1 Improved Side Chain Fit.

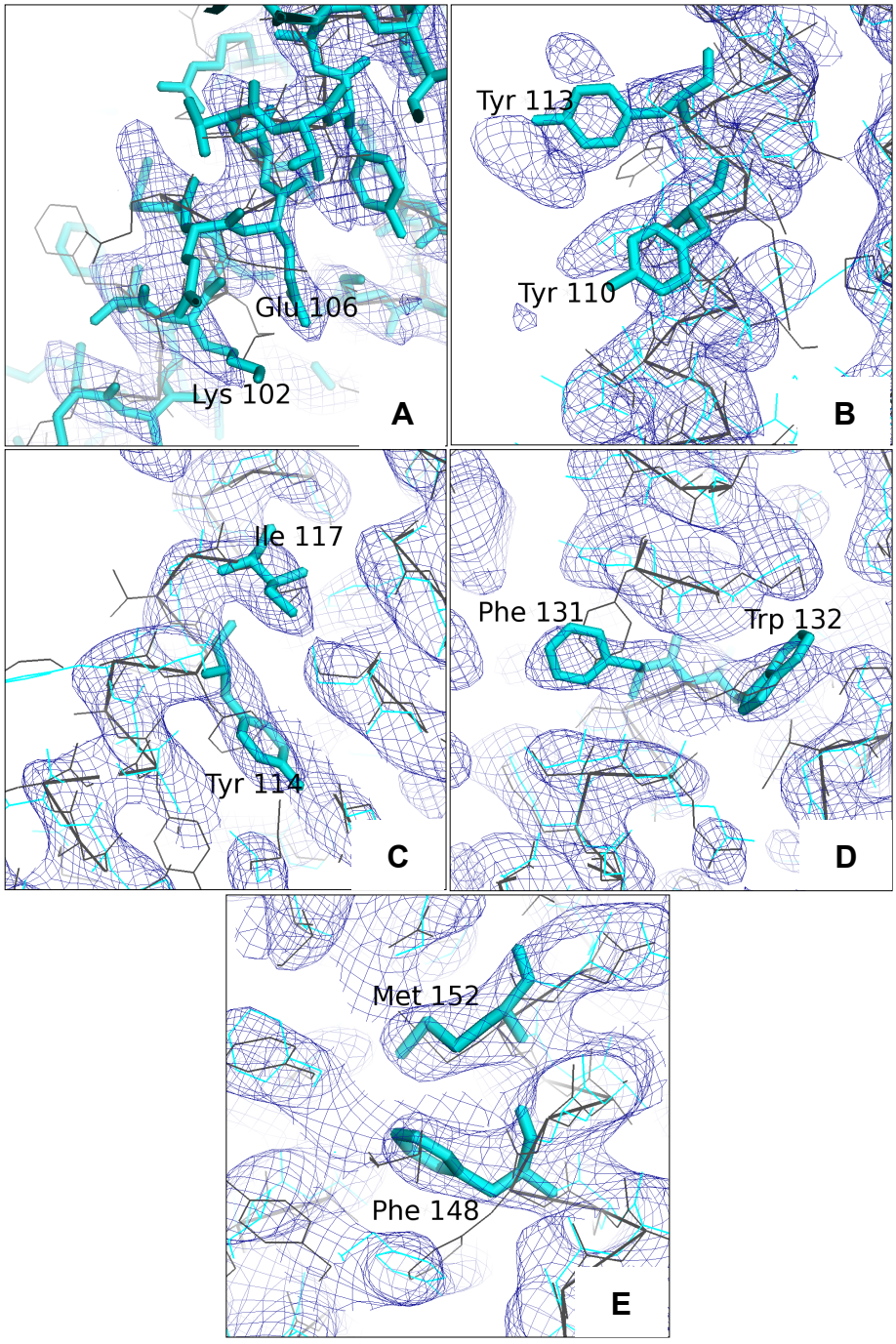

Figure S4. Improved Side Chain Fit for Transmembrane Helix 2.

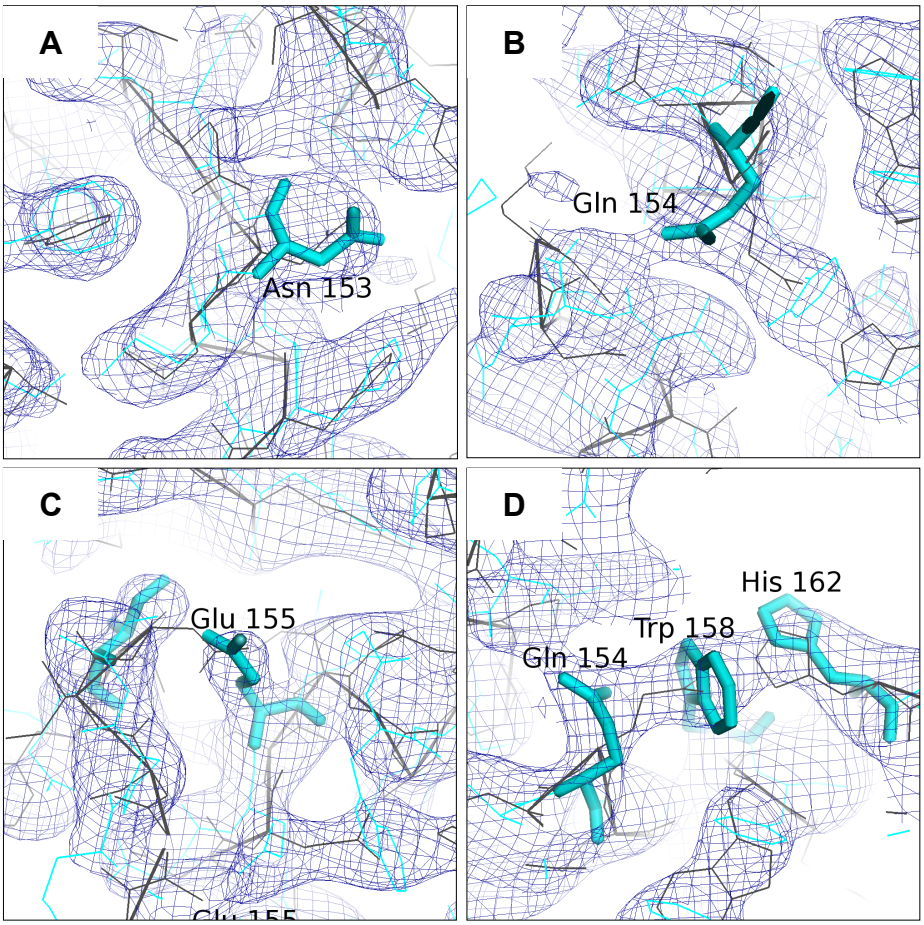

Figure S5. Significant Remodeling of Intracellular Helix 1.

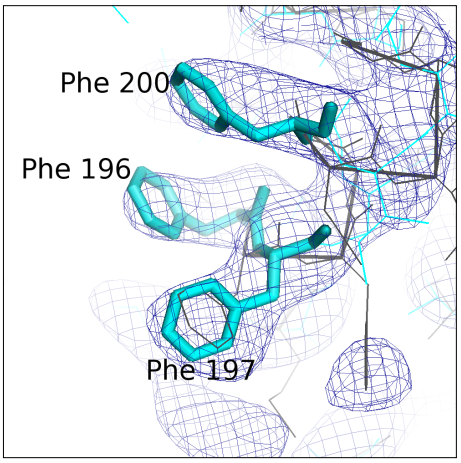

Figure S6. Registry Shift in Transmembrane Helix 3.

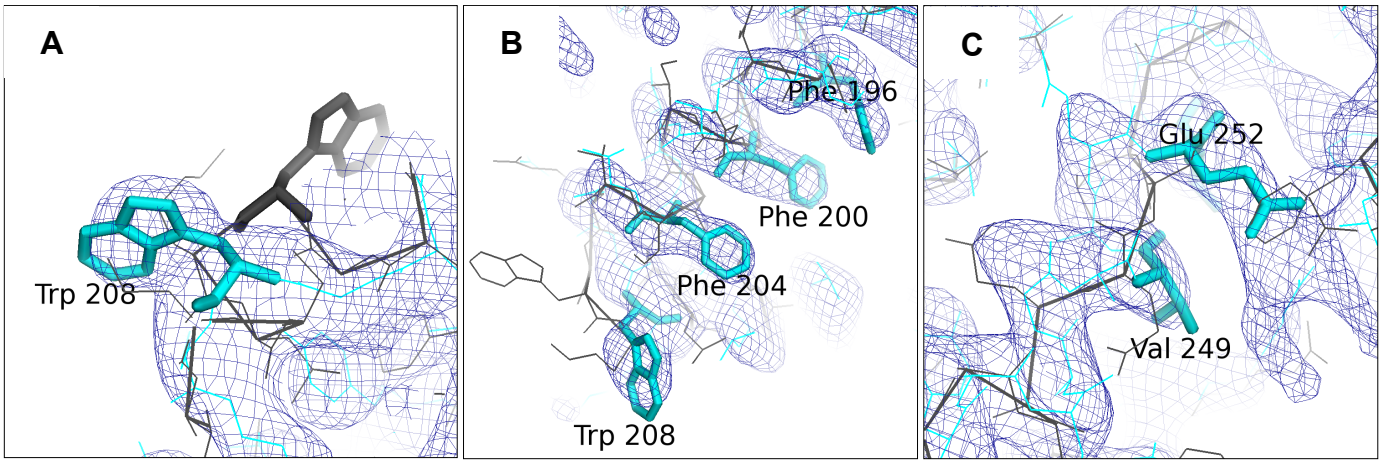

Figure S7. Remodeling of Extracellular Loop 2 and Transmembrane Helix 4 Results in Improved Fit of Side Chains.

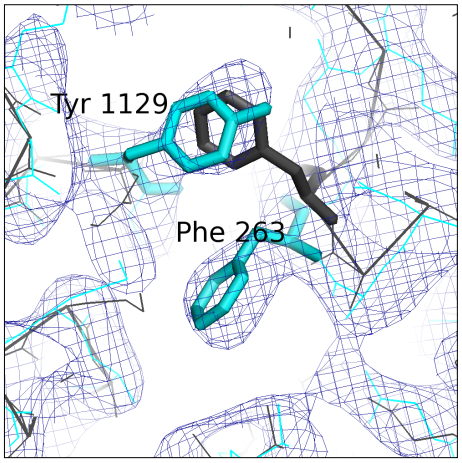

Figure S8. Improved Fit of Phe 263 Into Electron Density Compared To the Original Structure.

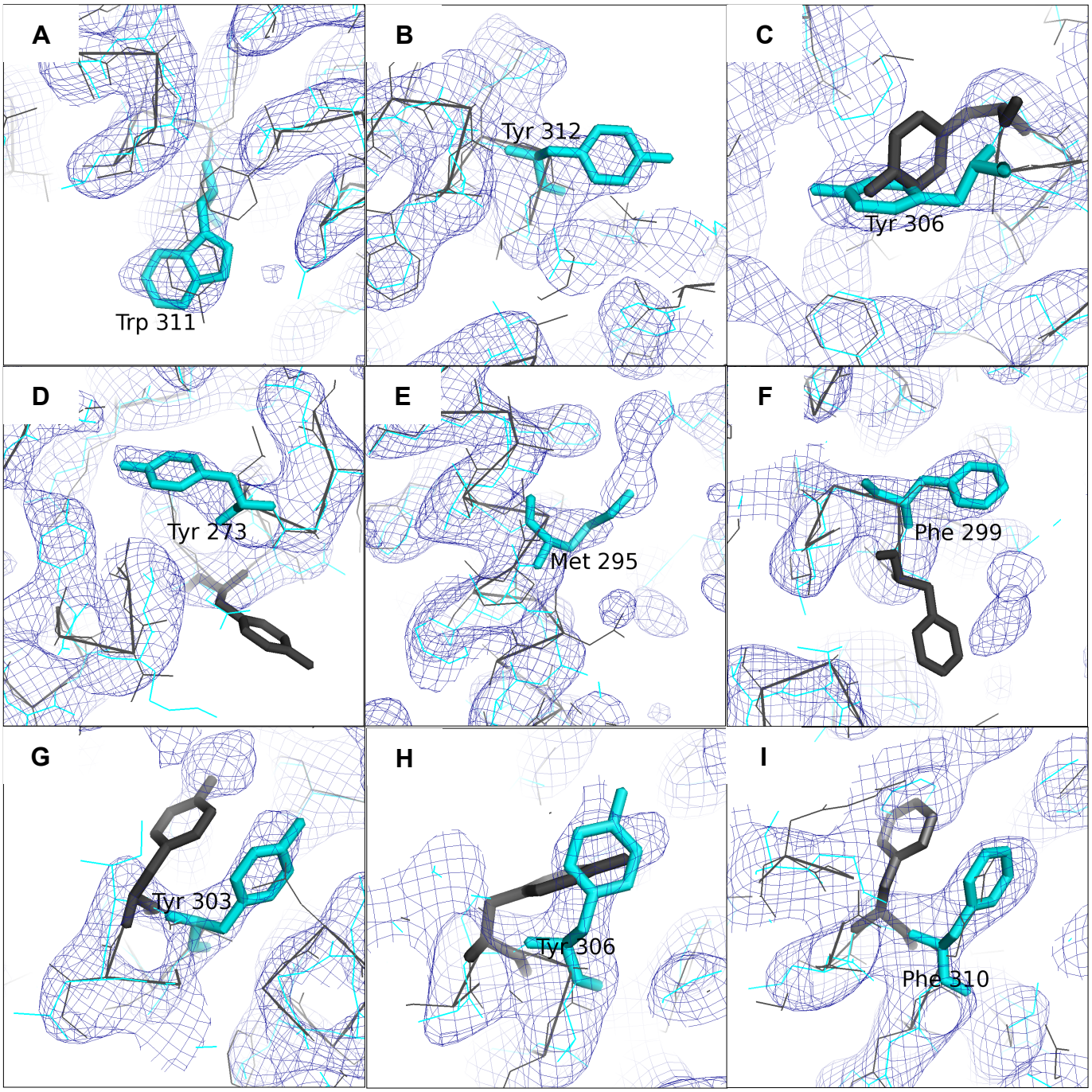

Figure S9. A 90° Shift in Registry for Transmembrane Helix 5 Results in Improved Fit for Multiple Side Chains.

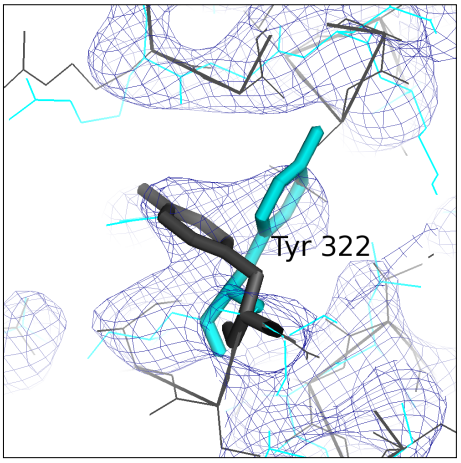

Figure S10. Improved Fit of the Backbone and Tyr 322 in Extracellular Loop 3.

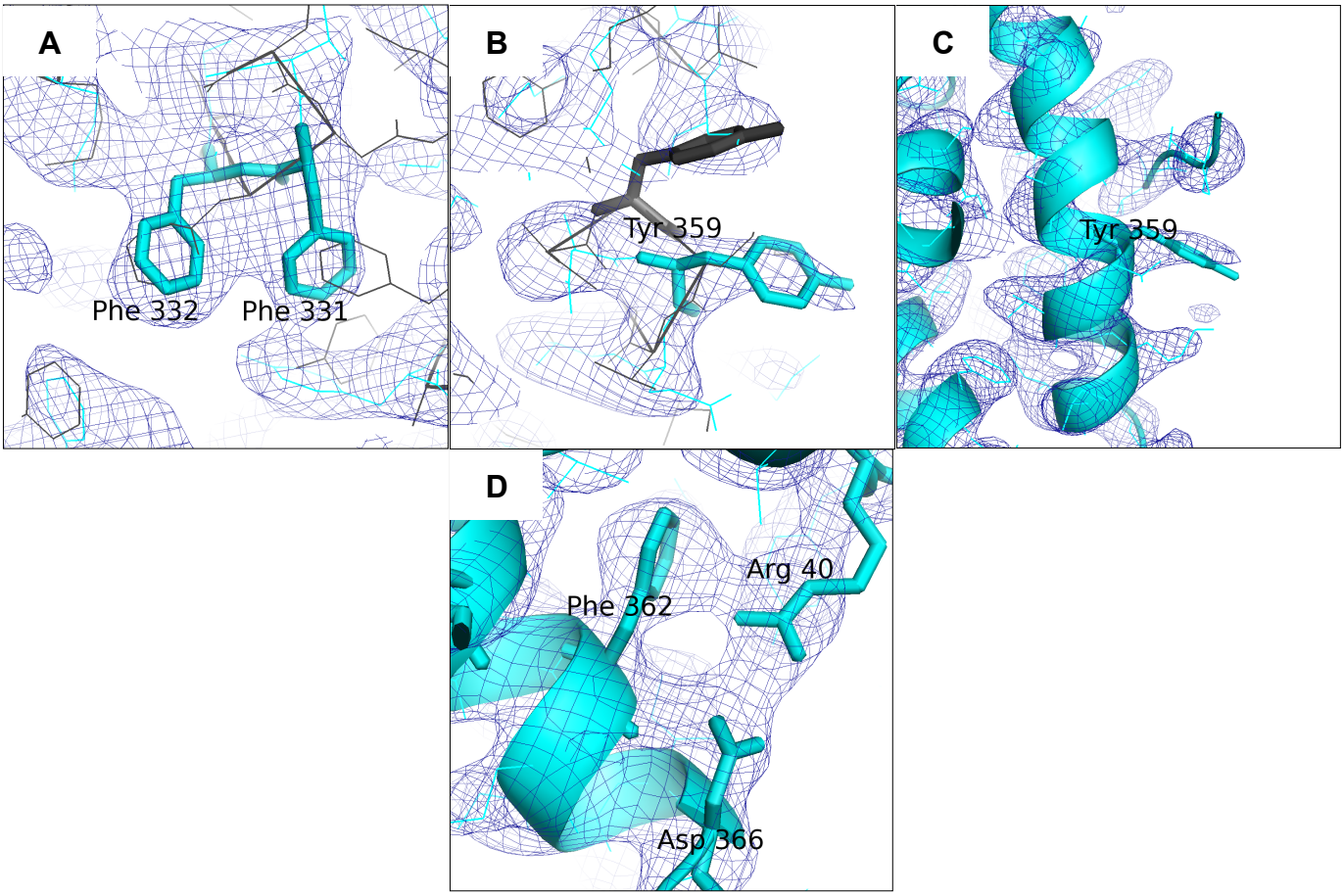

Figure S11. Tightening of Transmembrane Helix 6 Backbone Improves Fit of Several Side Chains.

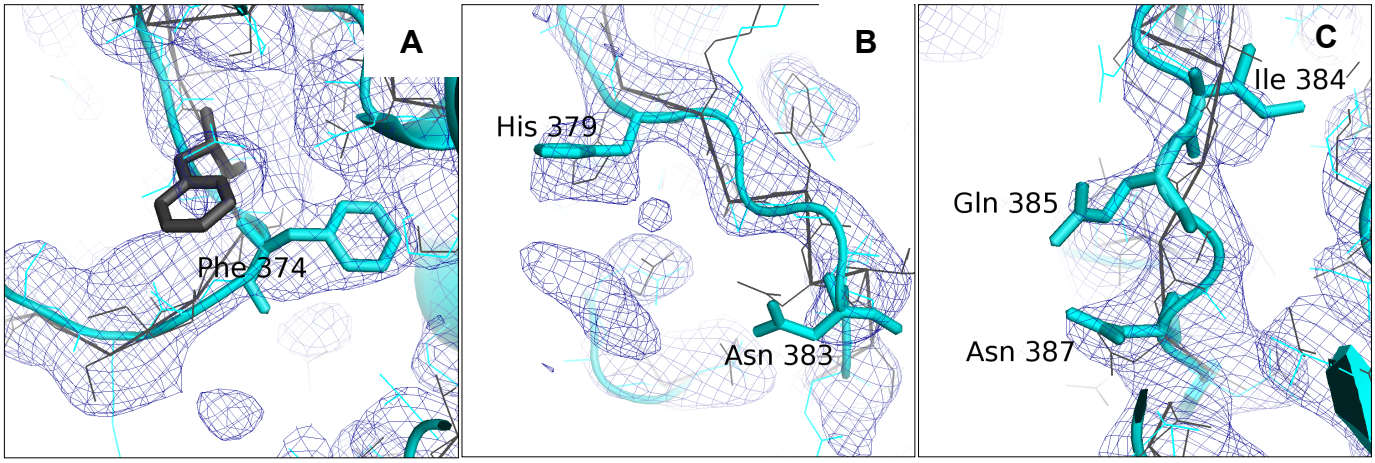

Figure S12. Complete Remodeling of the TM6-NBD1 Connector.

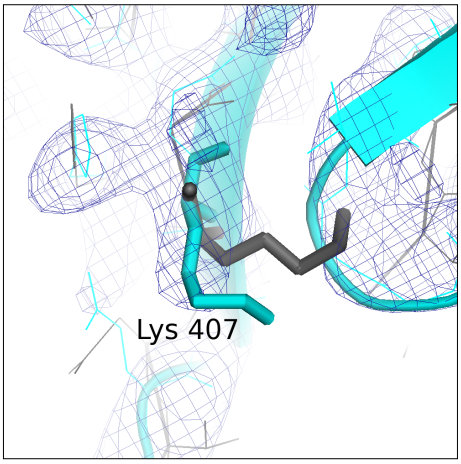

Figure S13. Improvement of Side Chain Fit in Nucleotide Binding Domain 1.

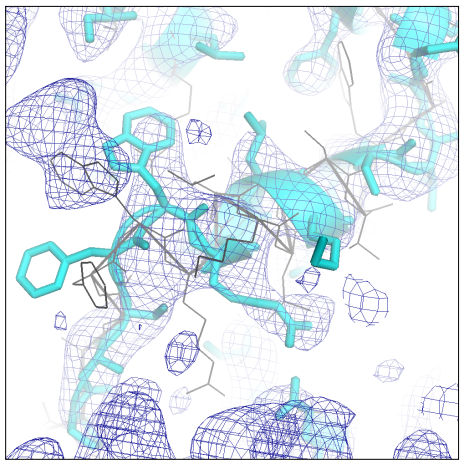

Figure S14. Remodeling of Elbow Helix 2 Improves Side Chain Fit.

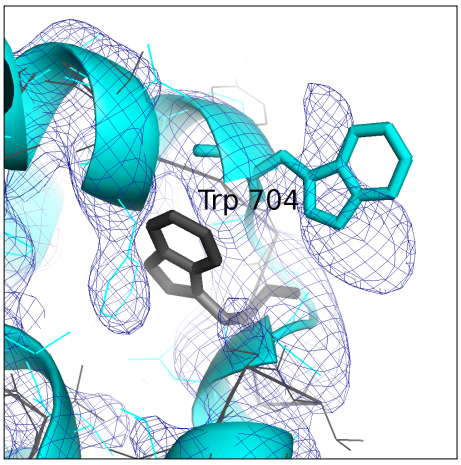

Figure S15. Remodeling of Transmembrane Helix 7 Allows Good Fit Into Electron Density.

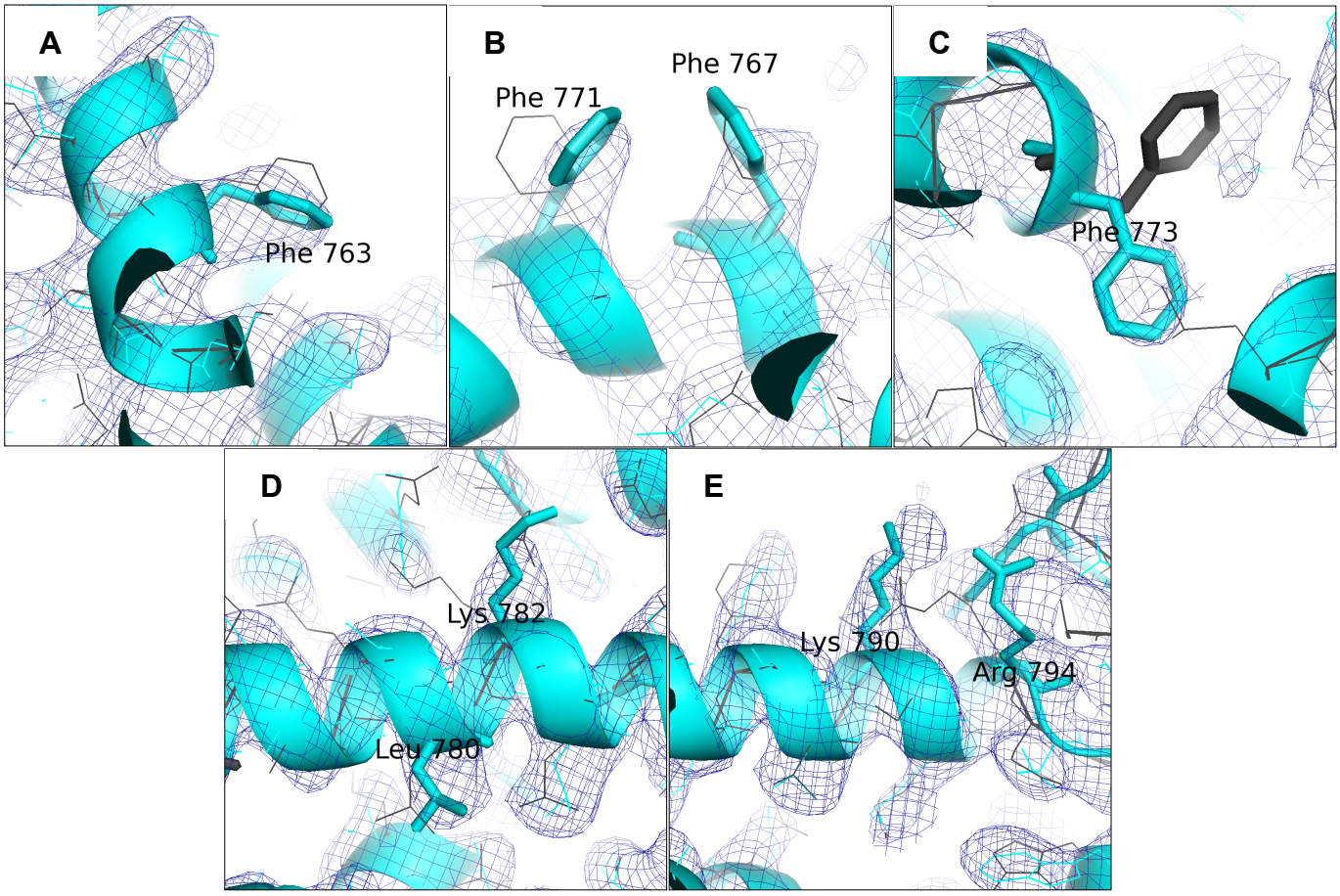

Figure S16. Improvement of Side Chain Fit in Transmembrane Helix 8.

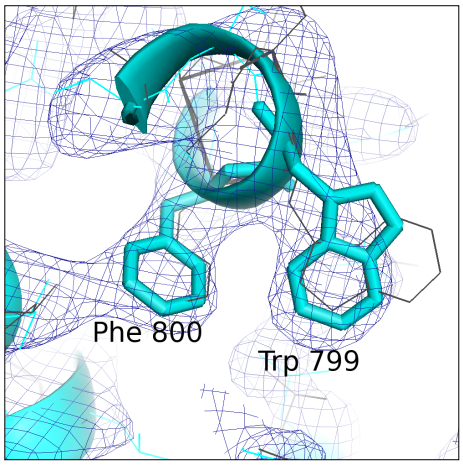

Figure S17. Remodeling of Intracellular Helix 3 Improves Side Chain Fit.

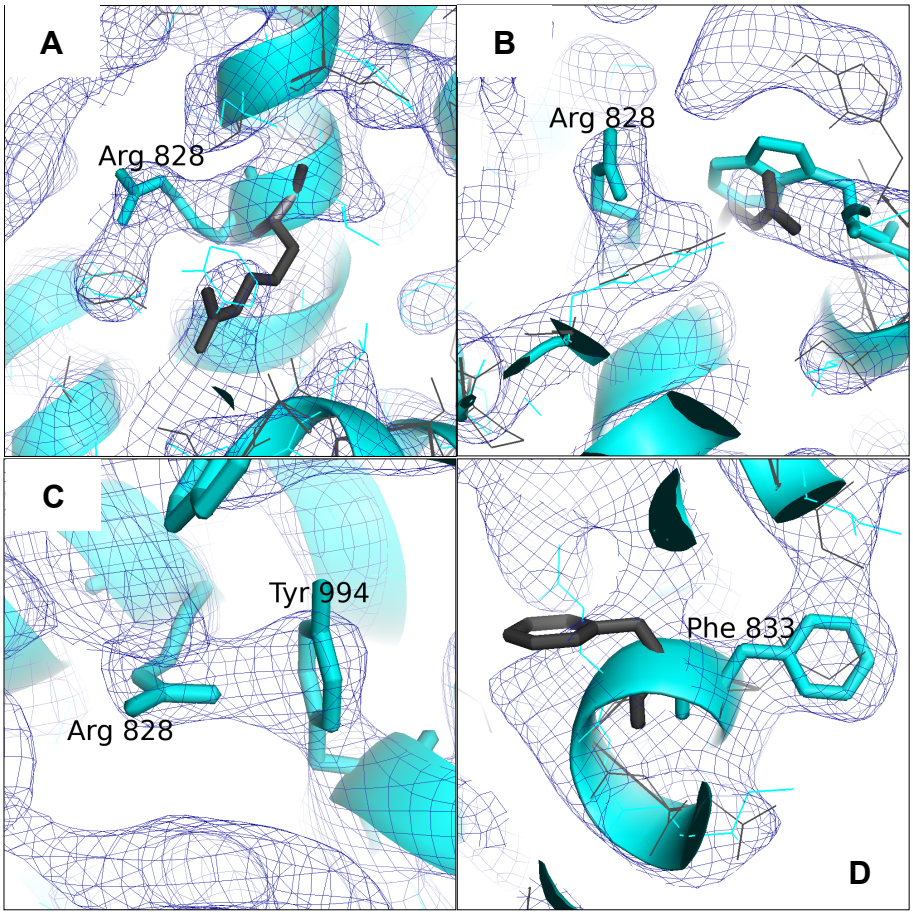

Figure S18. Relaxation of Transmembrane Helix 9 Improves Side Chain Fit and Eliminates Clash at Position 828.

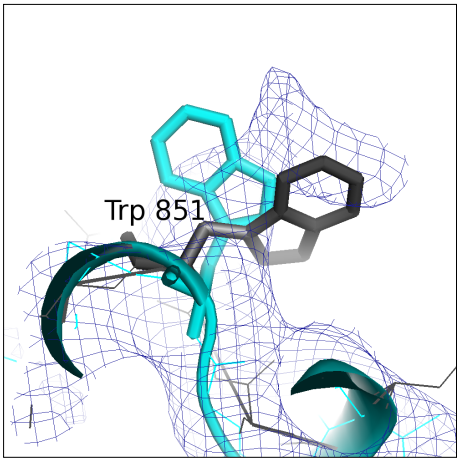

Figure S19. Improved Electron Density Fit for Extracellular Loop 5 and Side Chains.

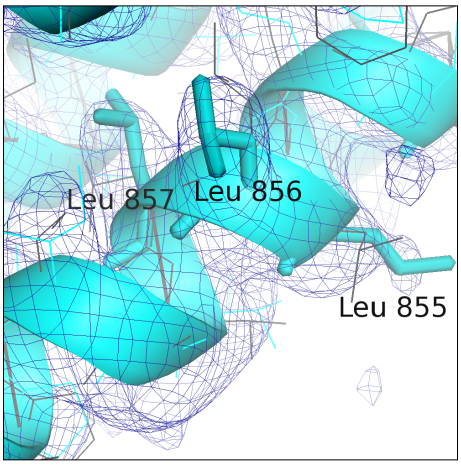

Figure S20. Improved Side Chain Fit for Transmembrane Helix 10.

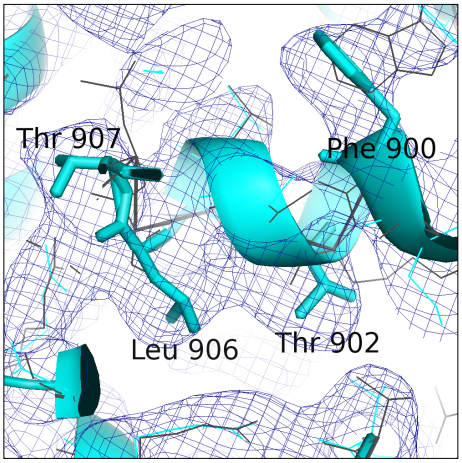

Figure S21. Remodeling of Intracellular Helix 4 residues 899-908.

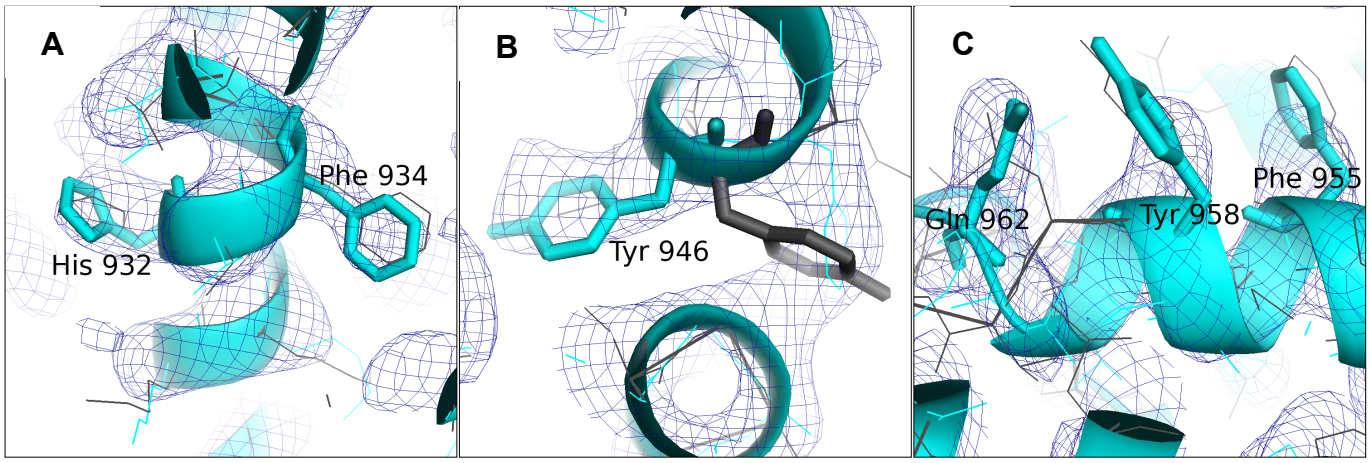

Figure S22. Improved Side Chain Fit for Transmembrane Helix 11.

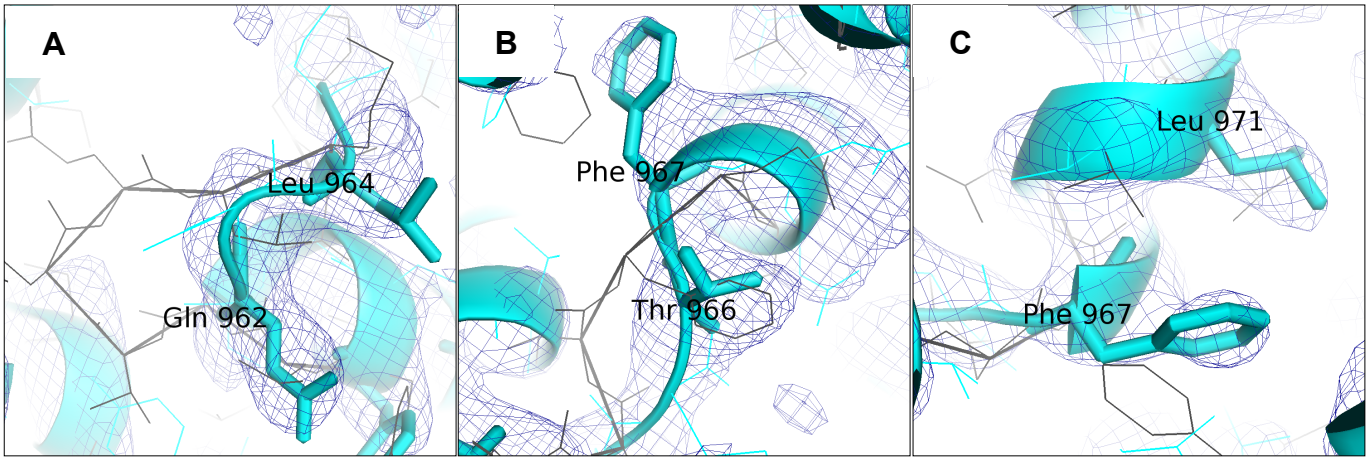

Figure S23. Backbone Remodeling of Extracellular Loop 6.

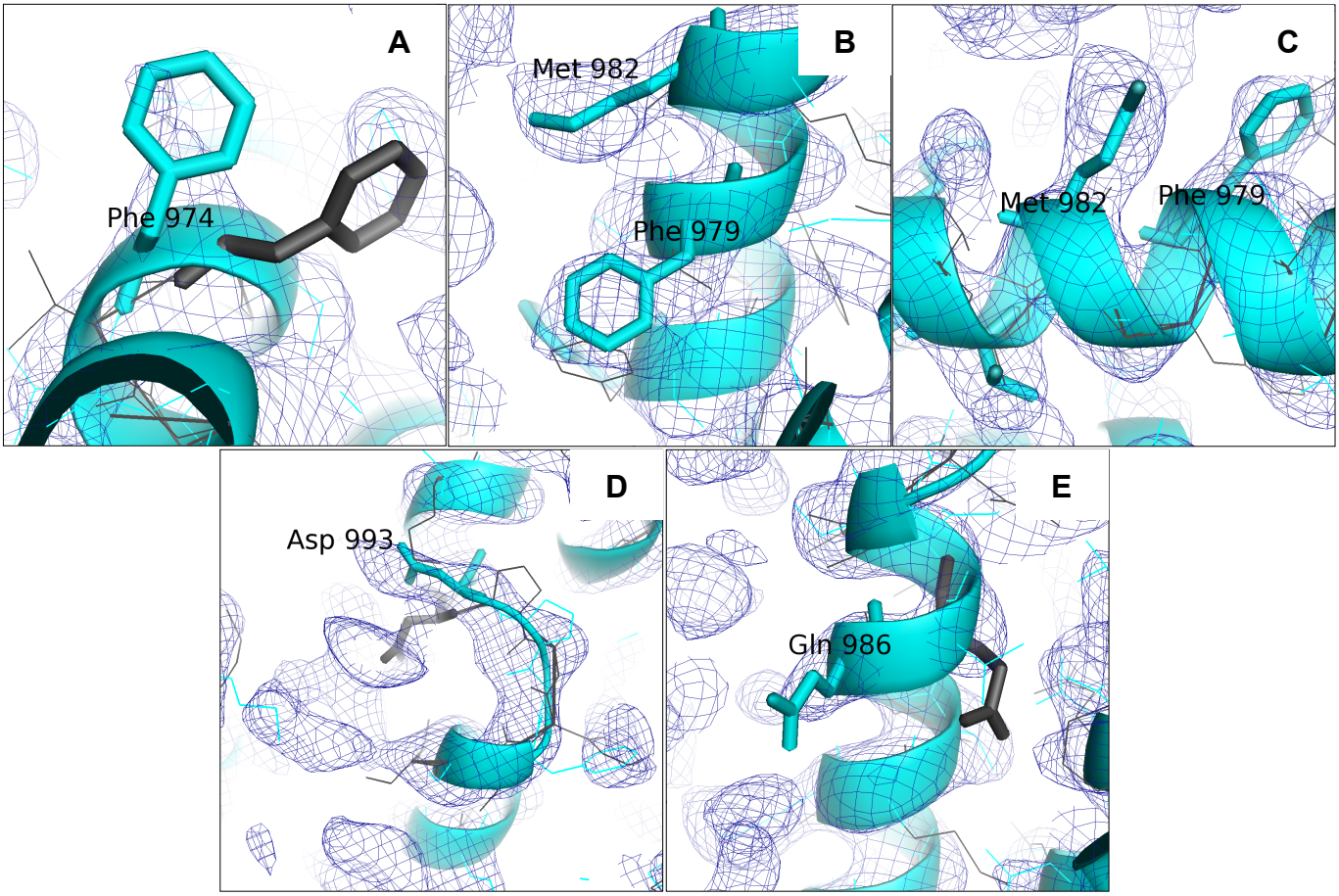

Figure S24. Transmembrane Helix 12 Registry Correction.

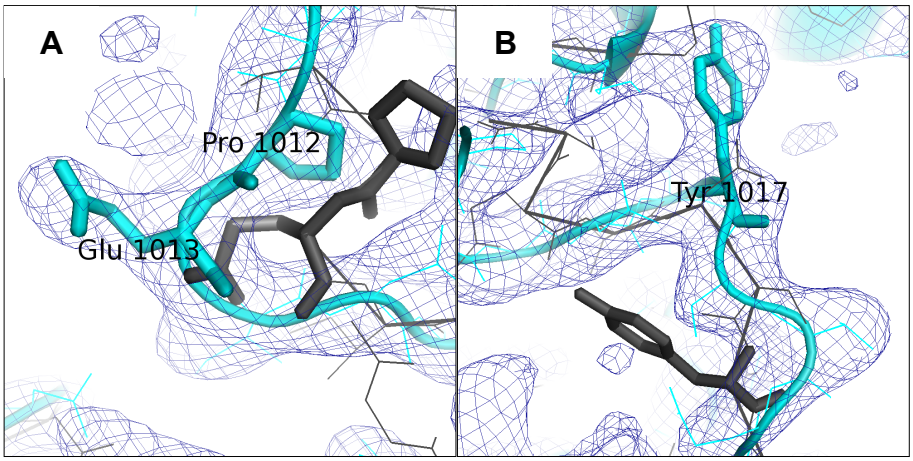

Figure S25. Improved Backbone and Side Chain Fit in the TM12-NBD2 connector.

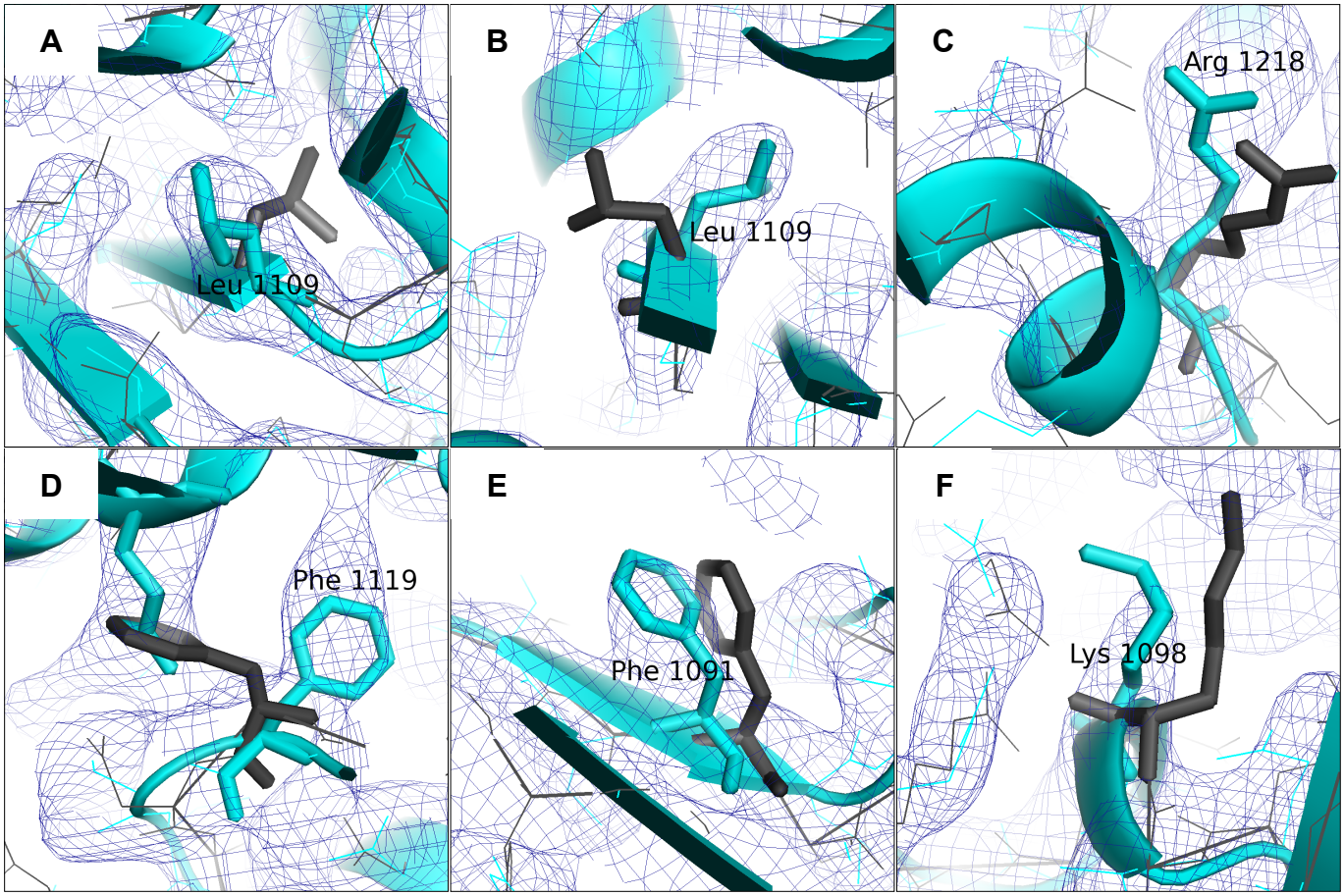

Figure S26. Improved Side Chain Fit in Nucleotide Binding Domain 2.

refinement	original (3G60) (QZ59RRR)	corrected (4M2S) (QZ59RRR)	original (3G61) (QZ59SSS)	corrected (4M2T) (QZ59SSS)
R_{work}	0.314 (0.421)[a]	**0.223 (0.261)[a]**	0.308 (0.460)[b]	**0.226 (0.251)[b]**
R_{free}	0.365 (0.472)[a]	**0.289 (0.325)[a]**	0.356 (0.498)[b]	**0.279 (0.319)[b]**
Clashscore, all atoms[c,d]	83.12 (16^{th})	**11.3 (97^{th})**	96.4 (13^{th})	**10.13 (97^{th})**
poor rotamers[c]	180 (9.2%)	**44 (2.25%)**	289 (14.8%)	**61 (3.12%)**
Ramachandran outliers[c]	338 (14%)	**21 (0.89%)**	370 (15.7%)	**13 (0.55%)**
Ramachandran favored[c]	1411 (60%)	**2204 (93%)**	1363 (58%)	**2196 (93%)**
Molprobity score[c,d,e]	4.04 (29^{th})	**2.27 (99^{th})**	4.27 (13^{th})	**2.35 (99th)**
C_β deviations[c]	3	**2**	4	**3**
bad backbone bonds[c]	1	**0**	0	**0**
bad backbone atoms[c]	56	**0**	53	**0**
R.m.s.d. bond lengths (Å)	0.008	**0.004**	0.008	**0.004**
R.m.s.d. bond angles (°)	1.500	**0.784**	1.600	**0.850**

Table S2. Refinement and Model Statistics for drug-bound structures of P-glycoprotein.
[a]Highest resolution bin (4.67 – 4.40 Å) is shown in parentheses.
[b]Highest resolution bin (4.62 – 4.35 Å) is shown in parentheses.
[c]http://molprobity.biochem.duke.edu (using electron-cloud x-H bond-lengths and no N/Q/H flips).
[d]Percentile score at the time of this publication is shown in parentheses.
[e]MolProbity score combines the clashscore, rotamer, and Ramachandran evaluations into a single

Translocation pathway residues			
mouse Pgp	human Pgp	*C. eleg.* PGP-1	drug
His 60	**His 61**	Thr 87	Verap.
Phe 71	**Phe 72**	Gln 98	RRR, SSS
Tyr 114	Tyr 118	Tyr 142	SSS
Phe 299	**Phe 303**	Gln 327	SSS
Tyr 303	Tyr 307	Phe 331	SSS
Tyr 306	Tyr 310	Phe 334	RRR, SSS
Phe 332	**Phe 336**	Ser 360	RRR, SSS
Phe 339	**Phe 343**	Met 367	Rhod., RRR, SSS
Phe 724	Phe 728	Tyr 771	RRR, SSS, Verap.
Phe 728	Phe 732	Phe 775	RRR, SSS
Phe 766	**Phe 770**	Ser 811	SSS
Phe 938	Phe 942	Tyr 983	Verap.
Tyr 949	**Tyr 953**	Asn 994	RRR, SSS
Phe 953	Phe 957	Tyr 998	SSS
Phe 974	**Phe 978**	Met 1021	RRR, SSS
Phe 979	**Phe 983**	Ile 1026	RRR, SSS

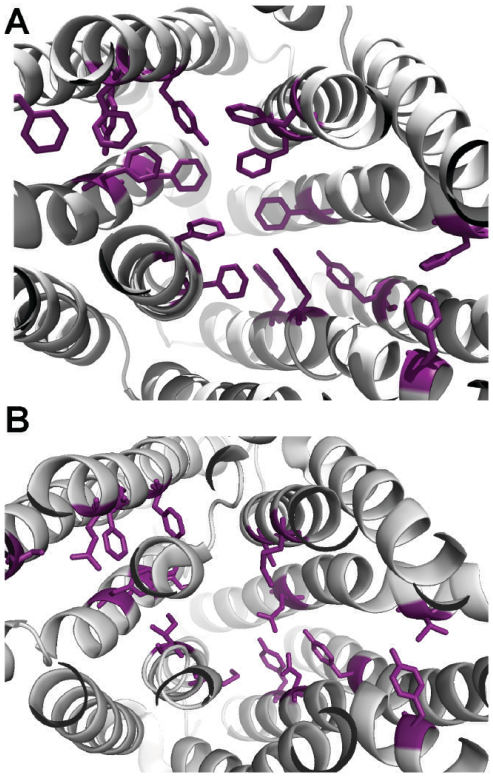

Figure S27. Composition of the P-glycoprotein Drug Translocation Pathway. Table: All 16 aromatic residues in the mouse- and human- Pgp drug translocation pathway are listed. Nine aromatic residues in mouse- and human- Pgp are not conserved in *C. elegans* PGP-1 (shown in bold). Drug column shows small molecules demonstrated to interact with mouse- and/or human- Pgp in the literature. Drug abbreviations: QZ59-SSS: "SSS", QZ59-RRR: "RRR", Verapamil: "Verap", and Rhodamine: "Rhod". **Panel A:** Amino acid side chains from the table are shown in purple for the improved structure of mouse Pgp, **Panel B:** The corresponding side chains for *C. elegans* Pgp are shown.

drug-binding residues			
mouse	human	CE	drug
His 60	**His 61**	Thr 87	verapamil
Ala 63	Gly 64	Gly 90	verapamil
Leu 64	Leu 65	Leu 91	RRR, SSS, verapamil
Met 67	Met 68	Met 94	SSS
Met 68	Met 69	Ser 95	RRR, SSS
Phe 71	**Phe 72**	Gln 98	RRR, SSS
Tyr 114	Tyr 118	Tyr 142	SSS
Val 121	Val 125	Met 149	verapamil
Ser 218	Ser 222	Thr 246	verapamil
Met 295	Ile 299	Phe 323	SSS
Phe 299	**Phe 303**	Gln 327	SSS
Ile 302	Ile 306	Asn 330	SSS, verapamil
Tyr 303	Tyr 307	Phe 331	SSS
Tyr 306	Tyr 310	Phe 334	RRR, SSS
Phe 332	**Phe 336**	Ser 360	RRR, SSS
Leu 335	Leu 339	Met 363	colchicine, SSS, verapamil, vinblastine
Ile 336	Ile 340	Met 364	RRR, SSS
Ala 338	Ala 342	Ser 366	verapamil
Phe 339	**Phe 343**	Met 367	rhodamine, RRR, SSS
Asn 717	Asn 721	Gly 764	SSS
Gln 721	Gln 725	Tyr 768	RRR, SSS
Phe 724	Phe 728	Tyr 771	RRR, SSS, verapamil
Ala 725	Ala 729	Ser 772	verapamil
Phe 728	Phe 732	Phe 775	RRR, SSS
Phe 766	**Phe 770**	Ser 811	SSS
Ala 837	Ala 841	Val 882	verapamil
Asn 838	Asn 842	Ser 883	verapamil
Ile 864	Ile 868	Val 909	verapamil
Ala 867	Ala 871	Gly 912	verapamil
Gly 868	Gly 872	Gln 913	verapamil
Phe 938	Phe 942	Tyr 983	verapamil
Thr 941	Thr 945	Ala 986	verapamil
Met 945	Met 949	Leu 990	SSS
Tyr 949	**Tyr 953**	Asn 994	RRR, SSS
Phe 953	Phe 957	Tyr 998	SSS
Leu 971	Leu 975	Leu 1018	colchicine, SSS, verapamil, vinblastine
Phe 974	**Phe 978**	Met 1021	RRR, SSS
Ser 975	Ser 979	Tyr 1022	RRR
Val 978	Val 982	Thr 1025	colchicine, RRR, SSS, verapamil, vinblastine
Phe 979	**Phe 983**	Ile 1026	RRR, SSS
Gly 980	Gly 984	Ser 1027	verapamil
Ala 981	Ala 985	Thr 1028	verapamil
Met 982	Met 986	Ser 1029	RRR, SSS
Ala 983	Ala 987	Thr 1030	RRR, SSS
Gln 986	Gln 990	Phe 1033	RRR, SSS
Val 987	Val 991	Ala 1034	SSS
95.7%	identity	13.0%	
100.0%	similarity	58.7%	

Table S3. Conservation of the P-glycoprotein Drug Translocation Pathway. Mouse and human Pgp are ~96% identical over 46 amino acid residues identified previously as interacting with drugs or those identified interacting with cyclic peptides in the corrected mouse Pgp structures. The same positions are only ~13% identical between *C. elegans*- and human Pgp. Mouse and human Pgp share nine pairs of aromatic residues in the drug translocation pathway (in bold) that are not conserved in *C. elegans* PGP-1. Residues deemed similar to human Pgp residues are colored blue. Residues colored red are dissimilar from human Pgp. The corresponding human and *C. elegans* residues were taken directly from the multiple sequence alignment published by Jin et al (*2*), Figure 9.

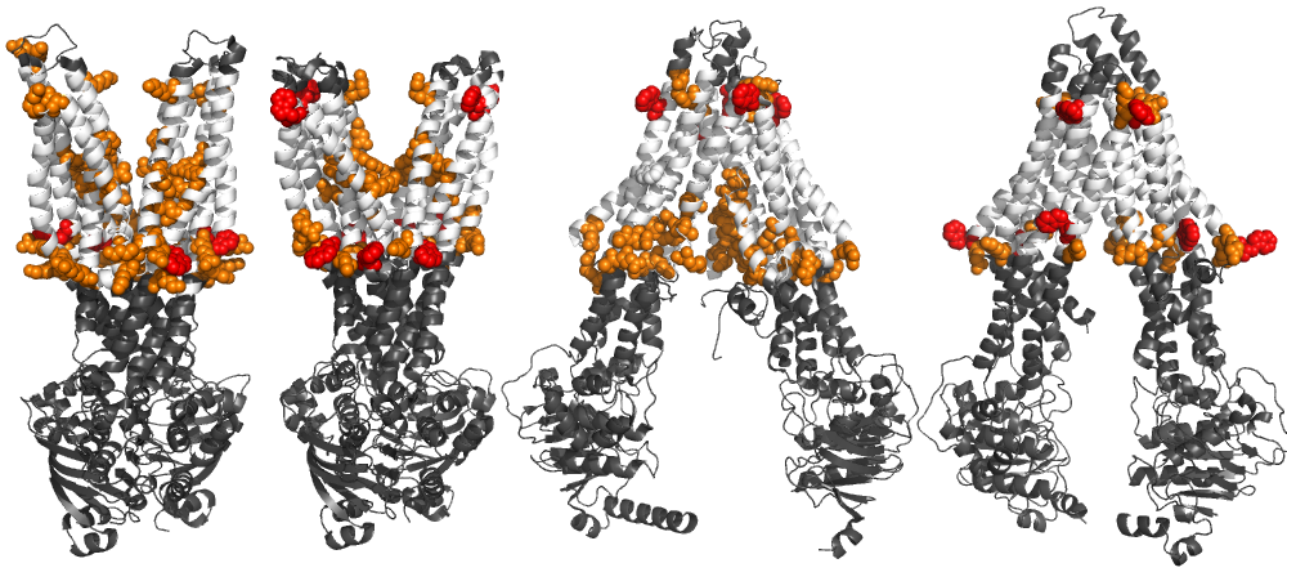

Figure S28. Distribution of Charged Amino Acid Residues in the Substrate Translocation Pathway of Lipid Flippases and Drug Transporters. From left to right: Sav1866, MsbA, *C. elegans* PGP-1 and mouse P-glycoprotein. Tryptophan residues used to delineate the position of the head groups of the bilayer (*3*) are shown in red. Amino acid residues bearing a formal charge (Arg, Lys, Asp, Glu) are shown in orange. Mouse P-glycoprotein contains no formal charges beyond the headgroup boundary of the lipid bilayer.

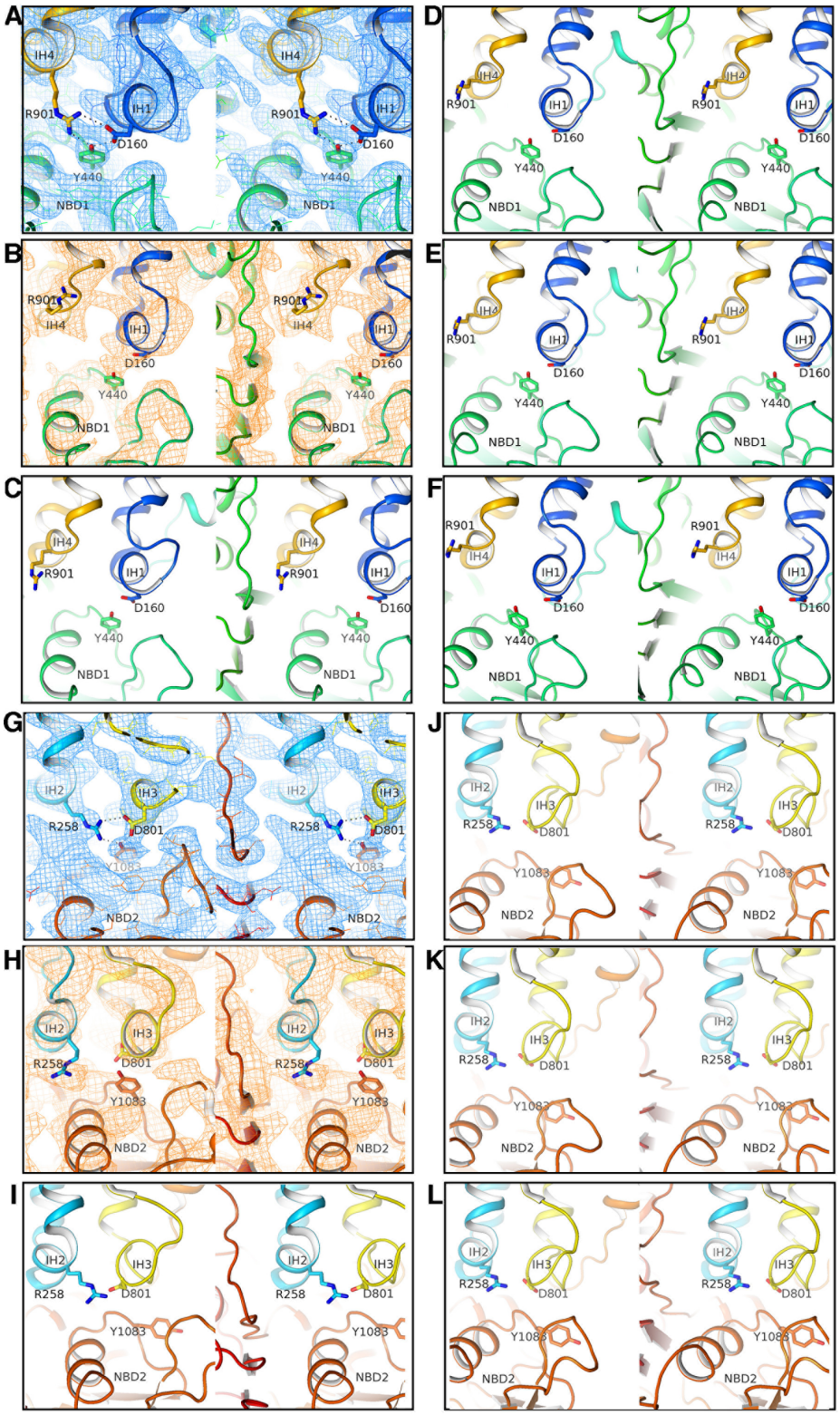

Figure S29. Modeling of the Conserved Salt Bridging between Intracellular Helices (IHs) and Nucleotide Binding Domains (NBDs) in mouse Pgp structures. Each boxed panel is rendered in wall-eyed stereo view. **Panels A-F** (top half of figure): zoom of IH1-IH4-NBD1 interface, **Panels G-L** (bottom half): zoom of IH2-IH3-NBD2 interface. **Panels A, G:** improved mouse Pgp structure (PDB 4M1M) with new SAD experimental electron density (blue mesh). **Panels B, H**: original mouse Pgp structure (PDB 3G5U) and original MAD experimental electron density map (orange mesh). **Panels C, I**: recent attempt to correct the original mouse Pgp structure with PDB entry only (PDB 4LSG) with no accompanying manuscript or data. **Panels D,J; F,K and J,L:** PDB codes 4KSB, 4KSC and 4KSD of recent mouse Pgp structures (*4*) slightly more open to the cytoplasm, similar to *C. elegans* PGP-1 (*2*).

Model / Map	4M1M / SAD map	3G5U / SAD map	4M1M / MAD map	3G5U / MAD map	4M1M / SAD unsharpened	4M1M / SAD over-sharpened
Overall map correlation	0.655	0.611	0.622	0.633	0.650	0.532
Correlation in region of model	0.715	0.659	0.700	0.702	0.709	0.582
Total residues	2368	2364	2368	2364	2368	2368
Residues in acceptable density	1436	1106	1215	1072	1415	1238
Residues with some weak density	932	1258	1153	1292	953	1130
Residues out of density	0	2	5	4	0	0
Residues in very weak density	55	73	72	91	65	54
Residues in weak density	348	485	474	522	348	362
Main-chain out of density	0	0	0	0	0	0
Main-chain in very weak density	3	5	0	0	3	3
Main-chain in weak density	66	71	76	66	65	97
Side-chain out of density	2	1	0	10	2	15
Side-chain in very weak density	31	47	4	74	29	50
Side-chain in weak density	222	395	251	452	225	263

Table S4. Cross-correlation analysis of models vs. experimental electron density maps. Correlation coefficients of models for the corrected mouse Pgp structure (4M1M) and the original structure (3G5U) were calculated for both the newly calculated single-anomalous dispersion (SAD) phased map and the original multi-wavelength anomalous dispersion (MAD) phased map. Values were achieved using phenix.get_cc_mtz_pdb. For comparison, an unsharpened (b_iso=0) SAD map (column labeled “SAD unsharpened”) exhibited very similar real space correlation to the corrected mouse Pgp modeled compared to the modestly sharpened map (“SAD map”; b_iso=-38) we used for modeling. Over-sharpening (“SAD over-sharpened”; b_iso=-78) resulted in less favorable correlation in real space.

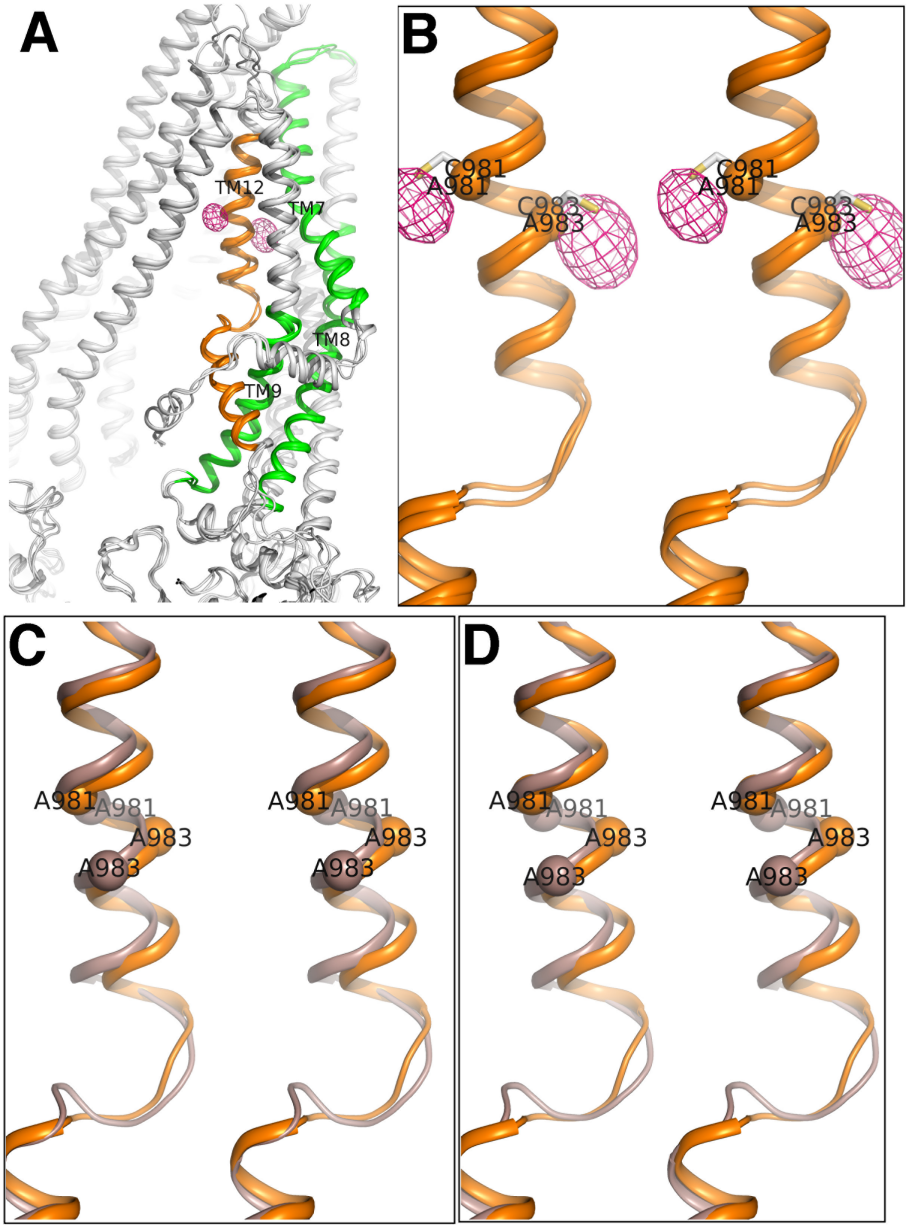

Figure S30. Incorrect Modeling of TM12 in Original and new PDB Entry 4LSG for mouse P-glycoprotein. **Panel A:** Superposition of four structures: original mouse Pgp (PDB code 3G5U), improved mouse Pgp structure (PDB 4M1M), an attempt to correct mouse Pgp (PDB 4LSG), and structure of the double mutant (A981C/A983C) labeled with mercury. TM12 is highlighted in orange. TM7 and a portion of TM8 & TM9 (residues 694:741; 760:794; 805:827 shown in green) were used to align 3G5U, 4LSG and 4M1M to the refined isomorphous (see Table S7 below) structure of A981C/A983C. These TMs were chosen to produce a highly precise alignment because the original structure contained no registry errors in this region. **Panels B-D:** wall-eyed stereo views. **Panel B:** Anomalous difference density for the mercury atoms (magenta density, contoured at 8 σ) of the double mutant (A981C/A983C) correspond precisely to the positions of A981 and A983 in our improved model of mouse Pgp (4M1M). **Panel C:** Registry error in the original modeling of TM12 (3G5U). **Panel D:** Registry error in the modeling of TM12 in 4LSG.

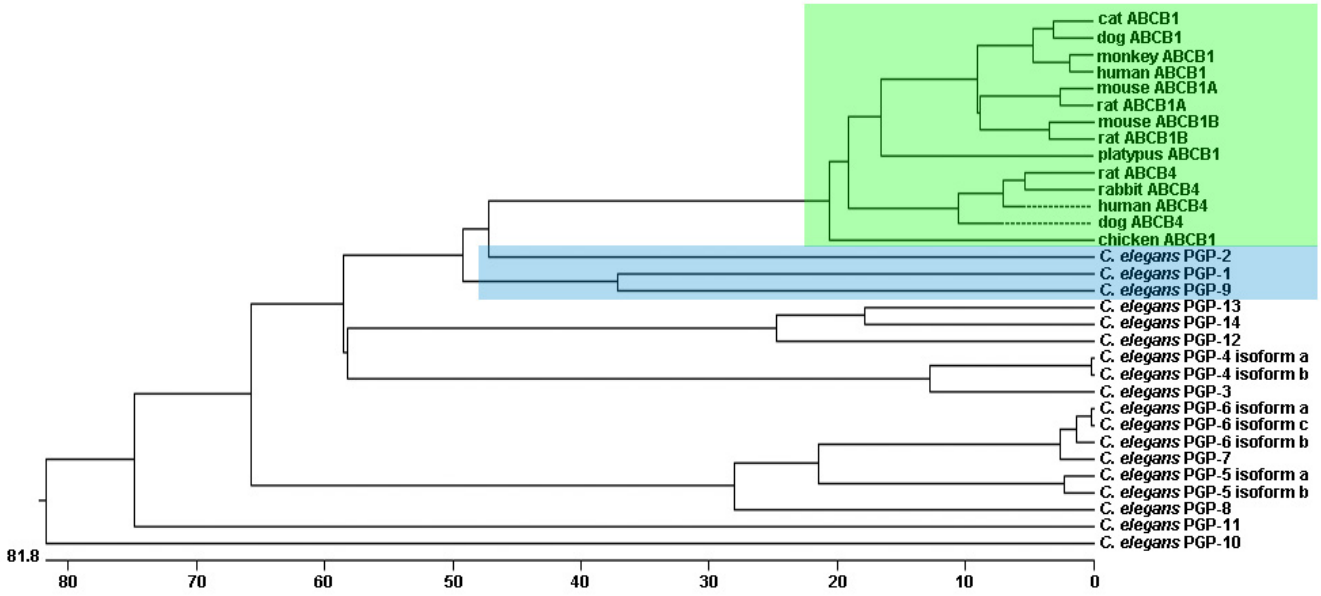

Figure S31. Phylogenetic analysis of P-glycoprotein. Vertebrate P-glycoprotein group into one tightly defined phylogenetic cluster (boxed in green) that is distinct from the many *C. elegans* PGP-X orthologs. *C. elegans* PGP-1, PGP-2 and PGP-9 (boxed in blue) are the closest of the nematode PGPs to be related to vertebrate Pgp, yet none is higher than 42% identity with any vertebrate Pgp. Chicken ABCB1, however is 70% identical to human Pgp, revealing a major jump in divergence in nematodes.

Model statistics	human Pgp model
Clashscore, all atoms[a,b]	6.75 (100th)
poor rotamers[a]	19 (0.97%)
Ramachandran outliers[a]	11 (0.47%)
Ramachandran favored[a]	2232 (95%)
Molprobity score[a,b,c]	1.73 (100th)
C_β deviations[a]	2
bad backbone bonds[a]	0
bad backbone atoms[a]	3
R.m.s.d. bond lengths (Å)	0.003
R.m.s.d. bond angles (°)	0.756

Table S5. Statistics for the Human Pgp Homology Model. A human Pgp model was created by sequentially mutating non-identical residues of mouse Pgp to the human Pgp sequence. The mutated model was then subjected to energy minimization and evaluated using MolProbity tools.
[a]http://molprobity.biochem.duke.edu (using electron-cloud x-H bond-lengths and no N/Q/H flips).
[b]Percentile score at the time of this publication is shown in parentheses.
[c]MolProbity score combines the clashscore, rotamer, and Ramachandran evaluations into a single value.

NCS GROUP 1			
OPERATOR 1			
CENTER:	33.4175	69.9998	22.4008
ROTA 1:	1	0	0
ROTA 2:	0	1	0
ROTA 3:	0	0	1
TRANS:	0	0	0
OPERATOR 2			
CENTER:	40.9511	50.8331	71.5554
ROTA 1:	0.1636	0.9725	0.1657
ROTA 2:	0.9649	-0.1927	0.1786
ROTA 3:	0.2056	0.1307	-0.9699
TRANS:	-34.574	27.5074	76.7397
NCS GROUP 2			
OPERATOR 1			
CENTER:	1.7916	90.4082	41.8376
ROTA 1:	1	0	0
ROTA 2:	0	1	0
ROTA 3:	0	0	1
TRANS:	0	0	0
OPERATOR 2			
CENTER:	64.6343	18.8097	56.8013
ROTA 1:	0.2116	0.9374	0.2767
ROTA 2:	0.9053	-0.2947	0.306
ROTA 3:	0.3684	0.1858	-0.9109
TRANS:	-45.2354	20.0588	66.2757

Table S6. NCS operators used in phasing restraints.

Data Processing	A32C	A216C/A244	A280C/A302	A981C/A983C
Source	APS 22-ID	APS 22-ID	APS 22-ID	CLS 08-ID
Space Group	P $2_12_12_1$	P $2_12_12_1$	P $2_12_12_1$	P $2_12_12_1$
Unit Cell	a= 99.1 Å, b= 119.5 Å, c= 379.2 Å,	a= 100.3 Å, b= 121.7 Å, c= 373.0 Å,	a= 101.2 Å, b= 121.9 Å, c= 380.0 Å,	a= 101.0 Å, b= 123.0 Å, c= 376.1 Å,
Wavelength (Å)	1.007	1.007	1.007	1.007
Resolution (Å)	5.3	5.4	5.9	5.6
Redundancy	6.4	3.0	4.3	3.6
R_{sym}[a], %	7.6	6.1	6.6	5.6
Completeness, %	93	92	91	98

[a] $R_{sym} = \Sigma|I-\langle I\rangle|\Sigma\langle I\rangle$, where I is the measured intensity of each reflection, and <I> is the intensity averaged from symmetry equivalents.

Table S7. Crystallographic Table of Mutants Labeled with Mercury for Validating Significant Changes to Mouse P-glycoprotein Structure.

References

1. S. G. Aller *et al.*, Structure of P-glycoprotein reveals a molecular basis for poly-specific drug binding. *Science* **323**, 1718 (Mar 27, 2009).
2. M. S. Jin, M. L. Oldham, Q. Zhang, J. Chen, Crystal structure of the multidrug transporter P-glycoprotein from Caenorhabditis elegans. *Nature* **490**, 566 (Oct 25, 2012).
3. M. Schiffer, C. H. Chang, F. J. Stevens, The functions of tryptophan residues in membrane proteins. *Protein engineering* **5**, 213 (Apr, 1992).
4. A. B. Ward *et al.*, Structures of P-glycoprotein reveal its conformational flexibility and an epitope on the nucleotide-binding domain. *Proc Natl Acad Sci U S A*, (Jul 30, 2013).